crystals

MDPI

*Article*

# Geometric Resonance Analysis of Superconductivity in $CaC_6$: Hexagonal and Rhombohedral Descriptions in the Roeser–Huber Framework

**Michael R. Koblischka [1,2,*] and Anjela Koblischka-Veneva [1,2]**

[1] Saarland University, P.O. Box 151150, 66041 Saarbrücken, Germany
[2] SupraSaar, 66133 Saarbrücken, Germany
* Correspondence: m.koblischka@gmail.com or m.koblischka@ieee.org

**Abstract**

The superconducting transition temperature of $CaC_6$ is investigated within the Roeser–Huber (RH) formalism using both rhombohedral and hexagonal crystallographic representations. While these two descriptions are crystallographically equivalent, they differ in their geometric construction of superconducting paths and near-atom environments. In the rhombohedral representation, only translationally closed Ca–Ca vectors consistent with the primitive lattice are considered, yielding three symmetry-distinct RH paths. In the hexagonal representation, the same superconducting channels are expressed in an expanded conventional cell, where some paths appear as unfolded or symmetry-related sublattice connections. For each representation, the RH path lengths and effective near-atom counts are evaluated and used to compute the superconducting transition temperature. The rhombohedral description yields $T_c^{(\mathrm{calc})} = 10.4$ K, while the hexagonal representation gives $T_c^{(\mathrm{calc})} = 10.9$ K, both in good agreement with the experimental value $T_c^{(\mathrm{exp})} = 11.5$ K. The difference between the calculated values amounts to approximately 5%. These results show that the underlying RH superconducting channels and their near-atom environments are representation independent, while minor quantitative differences in $T_c^{(\mathrm{calc})}$ arise from metric redistribution of equivalent paths. This directly confirms that the RH formalism captures intrinsic structural features of superconductivity rather than artifacts of unit-cell representation.

**Keywords:** g raphite intercalation compounds; $CaC_6$; superconducting transition; Roeser–Huber formalism; superconducting paths; geometric resonance



Academic Editors: Martin Dressel, António José Arsénio Costa, Jun Zheng, Elkin Ferney Rodriguez Velandia and João Filipe Pereira Fernandes

Received: 16 February 2026
Revised: 1 March 2026
Accepted: 7 March 2026
Published: 9 March 2026



## 1. Introduction

Graphite intercalation compounds (GICs) serve as prototypical systems for studying the interplay between layered electronic structure, charge transfer, and electron–phonon coupling. Early intercalation studies focused on alkali-metal compounds such as $LiC_6$, $KC_8$, and related phases, which exhibit metallic behavior but do not become superconducting at ambient pressure [1,2]; see also the review in Ref. [3]. In particular, $LiC_6$ represents the structurally closest analogue to $CaC_6$, sharing the same graphite host framework and similar staging, yet lacking superconductivity under comparable conditions. This contrast has motivated extensive theoretical and experimental efforts aimed at clarifying the microscopic mechanisms responsible for superconductivity in $CaC_6$ and related compounds [3].

The discovery of superconductivity in calcium-intercalated graphite ($CaC_6$) at a comparatively high transition temperature of $T_c \approx 11.5$ K stimulated renewed interest in layered

carbon-based superconductors [4–8]. Experimental investigations have characterized its phonon spectrum, isotope effect, Fermi-surface topology, and anisotropic superconducting properties, while density-functional theory (DFT) calculations have emphasized the role of interlayer Ca-derived electronic states and strong coupling to out-of-plane carbon vibrations [7,8]. $CaC_6$ thus occupies a central position in the study of phonon-mediated superconductivity in low-dimensional systems and provides a structurally simple yet electronically nontrivial testbed for theoretical models. Beyond its fundamental relevance, layered superconductors of this type are also important for understanding superconductivity in other graphitic and carbon-derived materials, including doped graphene and related intercalated structures.

The rapid development of two-dimensional superconducting materials has further intensified interest in graphite-derived systems [9–11]. In particular, Li-decorated graphene—effectively a monolayer analogue of $LiC_6$—has been predicted to exhibit superconductivity with a transition temperature of up to 8.1 K [12]. These findings underscore the importance of understanding how dimensionality, intercalant species, and lattice geometry collectively influence superconducting behavior in layered carbon systems.

$CaC_6$ can be viewed either as graphite with intercalated calcium atoms or, equivalently, as graphene sheets embedded within a calcium sublattice. Experimentally, $CaC_6$ is most commonly described using a conventional hexagonal unit cell that is three times larger than the primitive rhombohedral unit cell associated with space group $R\bar{3}m$ [5]. By contrast, many theoretical studies adopt the primitive rhombohedral representation, which reflects the minimal translational symmetry of the lattice (see, e.g., Refs. [13–16]). More recent works have explicitly compared the two representations of the $CaC_6$ lattice to improve the analysis of phonon dispersion measurements and to refine first-principles calculations [17–19].

Within this broader context, an important conceptual question arises: do structure-based approaches to superconductivity remain strictly invariant under changes in crystallographic representation? The Roeser–Huber (RH) formalism [20–22] provides an alternative interpretation of superconductivity in which the superconducting state emerges as a geometric resonance phenomenon governed by a characteristic spatial coherence length derived directly from crystallographic periodicities. As the RH construction relies explicitly on symmetry-allowed real-space paths and their geometric environment, $CaC_6$ constitutes an ideal test case: it combines structural simplicity, well-characterized superconducting behavior, and the availability of two commonly used yet metrically distinct unit-cell descriptions.

In this work, the RH framework is applied consistently to both the rhombohedral and hexagonal descriptions of $CaC_6$. By analyzing the symmetry-allowed superconducting Ca–Ca paths in each representation, we examine whether geometric path identification, near-atom counting, and the resulting resonance condition depend on the chosen unit cell. Although the hexagonal and rhombohedral descriptions are crystallographically equivalent, they differ in their explicit metric representation and therefore provide a stringent test of the representation invariance of geometry-based superconductivity models. Establishing such invariance is essential if structure-derived descriptors are to be employed systematically—for example, in comparative studies across graphite intercalation compounds, including $LiC_6$ and related phases, or in data-driven materials-screening approaches.

Within the RH formalism, superconductivity is described in terms of symmetry-allowed real-space paths connecting equivalent atoms of the superconducting sublattice. As discussed previously in Ref. [23], in the case of $CaC_6$, only Ca–Ca connections are assumed to carry the superconducting wave, whereas carbon atoms act exclusively as near or blocking atoms that influence the superconducting paths through phonon-mediated interactions.

A superconducting path of length $x$ is considered RH-allowed if it:

(1) connects symmetry-equivalent calcium atoms,
(2) is not blocked by atoms lying directly on the path,
(3) exists as a symmetry-equivalent set throughout the crystal.

The path symmetry is a very crucial point: any asymmetry introduces phase disruption due to uneven forces acting on the carriers. Furthermore, it must be guaranteed that the path continues throughout the crystal, enabling the charge-carrier wave to propagate through the entire superconducting material. Atoms surrounding a given superconducting path are counted as near atoms ($N_A$) if they satisfy either a geometric proximity criterion or a refined standing-wave criterion that accounts explicitly for the layered character of the structure. This will be discussed in detail in Section 2 below.

The present manuscript is organized as follows: In Section 2, the elements of the Roeser–Huber resonance condition for alloys and compounds are outlined. Section 3 introduces the crystal structure and electronic configuration of $CaC_6$, and the superconducting paths for the rhombohedral representation of $CaC_6$ are identified. In Section 4, the superconducting paths in the hexagonal description are summarized. Section 5 illustrates the mapping between rhombohedral and hexagonal superconducting paths. Section 6 discusses the metric dependence of the RH path counting and the importance of this procedure for possible implementation in machine-learning software. Finally, Section 7 presents our conclusions.

## 2. Roeser–Huber Resonance Condition

A detailed discussion of the Roeser–Huber (RH) formalism, as applied to various elements and alloys, has been presented previously in Refs. [21,22]. Therefore, we summarize here only the most relevant steps.

Superconductivity in the RH formalism is seen as a resonance effect between the charge carrier wave formed by Cooper pairs with the de Broglie wavelength, $\lambda_{cc}$, which moves through the crystal lattice. The RH framework postulates that the superconducting transition corresponds to the lowest standing-wave resonance of paired charge carriers confined to an effective path length, $x$. This picture can be straightforwardly understood when interpreting the superconducting transition seen in a resistance measurement as an integrated resonance curve. The underlying physics is given by the particle-in-box (PiB) principle of quantum mechanics [24].

The lowest energy level and the superconducting transition temperature are given by [21,22]

$$\Delta_{(0)\mathrm{ges}} = \frac{h^2}{2M_\mathrm{L}} \cdot \left( \sum_{i=1}^{n} \frac{1}{(2x_{R_i})^2} \cdot \frac{n_{2R_i}}{n_{1R_i}} \right) = \pi k_B T_{c(0)}^{\mathrm{calc}}, \tag{1}$$

where $k_B$ = Boltzmann's constant, $h$ = Planck's constant, and $M_L = \eta \cdot 2m_e$, with $m_e$ denoting the free electron mass. $\eta$ is a parameter reflecting the Fermi and Debye temperatures of the material, yielding $\eta = 918.1$ [23]. According to the resonance view, $T_c^{\mathrm{calc}}$ corresponds to the mean field $T_c^{\mathrm{MF}}$ determined by the maximum of the derivative, $\mathrm{d}R/\mathrm{d}T$.

The effective resonance length, $x$, is defined purely by geometric considerations. For each crystallographic direction $R_i$—hereafter referred to as a superconducting path—the two factors, $n_1$ and $n_2$, must be determined to obtain a complete description of the energy $\Delta_{(0)}$ and the corresponding transition temperature, $T_{c(0)}$. The parameter $n_1 = N_L/N_A$ is defined as the ratio of $N_L$, the number of electrons participating in the superconducting state, to $N_A$, the number of passed, near atoms encountered along the superconducting path within the crystal lattice. In Refs. [20–22], atoms were counted as "near" when the condition $l_{\mathrm{calc}}/x \leq 0.5$ was fulfilled. The parameter $l_{\mathrm{calc}}$ represents the perpendicular

distance of an atom to the selected superconducting path. Thus, the passed, near atoms must be searched within a cylinder around the vector $x$ with radius $l_{\text{calc}}$. For more complex lattices, a standing sinusoidal wave model for the Cooper-pair de Broglie wavelength was introduced in Ref. [23]:

$$l_{\text{calc}} \leq \frac{1}{2} x \sin\left(\frac{h_E}{x}\pi\right) \tag{2}$$

and

$$0 \leq h_E \leq \frac{\pi}{2}, \tag{3}$$

with $h_E$ denoting the distance of the plane in which the passing atoms are located to the atom from which the superconductivity originates. Thus, for $CaC_6$ with the presence of several graphene layers, both criteria must be evaluated.

The second parameter, $n_2$, characterizes the relation between symmetry-equivalent paths oriented along the same crystallographic direction. The factor $n_2$ becomes particularly important in complex superconducting structures where multiple superconducting paths coexist and are associated with different atomic species. Both parameters must be evaluated for each possible superconducting path. For $CaC_6$, this situation does not arise, since superconductivity is assumed to be carried exclusively by the calcium sublattice. Consequently, only a single type of superconducting path is present, and therefore $n_2 = 1$. In this way, the longstanding idea of directly linking superconductivity to the underlying crystal lattice [25] finds a natural realization within the RH framework.

It should be noted that the superconducting pairing interaction may involve multiple phonon modes (vibrational modes of the lattice), each contributing differently to the overall electron–phonon coupling. Such behavior is characteristic of complex crystal structures; for example, the graphite intercalation compounds (GICs) [3] and A15-type [26] superconductors, where several optical and acoustic phonon branches interact with the conduction electrons. Within the RH framework, this multimode phonon coupling is effectively incorporated through the counting of the near, passed atoms along a given superconducting path, which serves as a geometric measure of the local vibrational environment experienced by the superconducting wave.

The required crystallographic data come from respective databases [27–29], enabling the RH formalism to be integrated straightforwardly into machine learning frameworks for predictive superconductivity studies [30–33].

## 3. Crystallographic Background of $CaC_6$

$CaC_6$ is the only member of the GIC with a rhombohedral unit cell (space group R$\bar{3}$m) with the lattice parameters $a = b = 0.517$ nm, $\alpha = 49.55°$ [5]. This primitive rhombohedral contains a single calcium atom and six carbon atoms per unit cell. The carbon atoms form a graphitic planar hexagon located in the median plane of the cell with an in-plane C–C distance of approximately 1.42 Å, which is very close to the C–C bond length in pristine graphene or graphite. In contrast, the calcium atom occupies a special Wyckoff position at the origin:

Carbon: 6 atoms 6g (1/6 5/6 1/2)
Calcium: 1 atom 1a (0 0 0)

This information enables the plotting of the structure using software like Crystalmaker [34] or VESTA [35]. The primitive rhombohedral cell is correct for symmetry analysis, but it does not allow for searching superconducting paths following the RH logic. Thus, the construction of supercells is required.

In Ref. [5], another representation of the rhombohedral cell was given (their Figure 7), which is now often used in the literature. However, we must note here that this figure is

not a direct real-space plot of a CIF unit cell. Instead, it represents a schematic symmetry diagram, which is drawn in a projected metric, emphasizing Wyckoff connectivity and topology. However, it is *not* intended to preserve Euclidean angles or lattice vectors. Having this in mind, one can carefully look at this figure to visualize some of the important channels for the path analysis. Figures 1A,B show the commonly used rhombohedral representation of $CaC_6$; in (A), the full cell is shown, and (B) gives the view in the [111]-direction. While this diagram reflects the correct symmetry, it is a schematic projection rather than a strict Euclidean representation of the primitive rhombohedral cell.

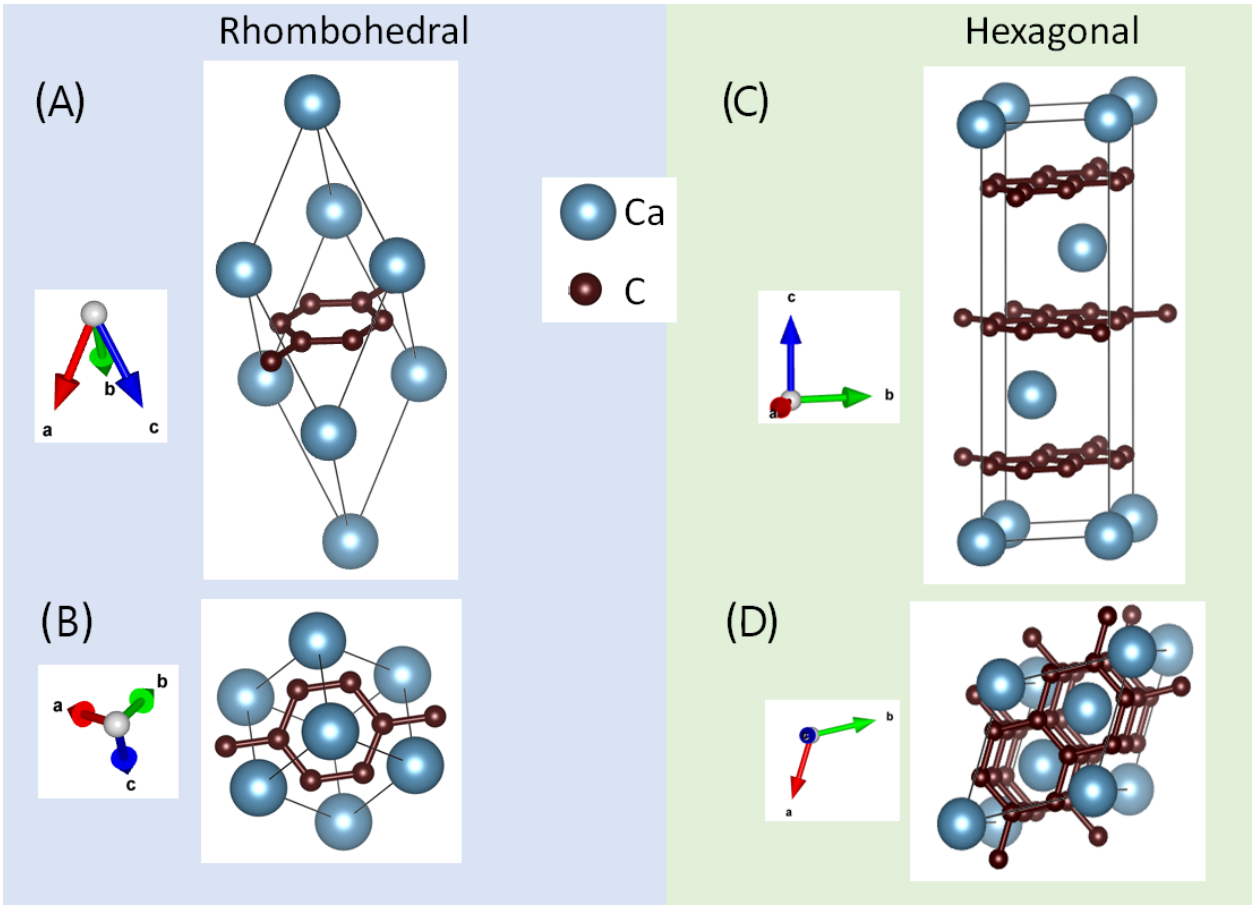


**Figure 1.** (**a**,**b**,**c**): The superconducting paths (1)–(3) for the rhombohedral unit cell of $CaC_6$. (**A**,**B**) give the rhombohedral unit cell of $CaC_6$ as drawn first by Emery et al. [5]. One must note here that this is not the primitive cell, see text. (**A**) is a view along the [001]-direction, which is often seen in the literature, and (**B**) gives the cell slightly off in the [111]-direction. (**C**,**D**) present the hexagonal cell of $CaC_6$ illustrating the graphene layers and the stacking of the Ca atoms. (**D**) shows a view slightly off the [001]-direction, enabling the view of channel-like arrangements.

In contrast, rhombohedral crystals are often represented using a hexagonal unit cell that is three times larger in volume. In this description, the lattice parameters of $CaC_6$ are $a = 0.4333$ nm and $c = 1.3572$ nm. Since the interlayer spacing between carbon sheets is $d = 0.4524$ nm, we obtain $c = 3d = 1.3572$ nm. In this representation, the shortest Ca–Ca distance in the intercalant layer is $a = 0.4333$ nm, and the closest C–C distance is $d_{CC} = 0.1444$ nm. The Wyckhof positions for this hexagonal structure were determined in Ref. [5] as follows:

Carbon: 18 atoms 18g (1/3 0 1/2)
Calcium: 3 atoms 3a (0 0 0)

Slightly different values were reported by Wang et al. [18], with $a = 0.43054$ nm and $c = 13.1205$ nm. This hexagonal $CaC_6$ cell is shown in Figure 1C (view along [100]) and Figure 1D (view slightly off the [001]-direction).

### 3.1. Superconducting Paths in Rhombohedral $CaC_6$

As mentioned before, only Ca–Ca vectors are considered as potential superconducting paths, whereas carbon atoms act exclusively as near, passed or blocking atoms. As consequence, superconducting paths necessarily connect calcium atoms in neighboring unit cells, as the rhombohedral unit cell contains only one Ca atom. The allowed paths are therefore determined by the symmetry-equivalent lattice vectors of the rhombohedral Bravais lattice.

### 3.2. Rhombohedral Edge Path

The shortest superconducting path in rhombohedral $CaC_6$ is directed along the edge of the rhombohedral unit cell. This path connects the calcium atom at the origin to an equivalent calcium atom in a neighboring cell along one of the three rhombohedral basis vectors, shown in Figure 2A. The path length is

$$x_{R1} = a_{rh} \approx 0.517 \text{ nm}. \quad (4)$$

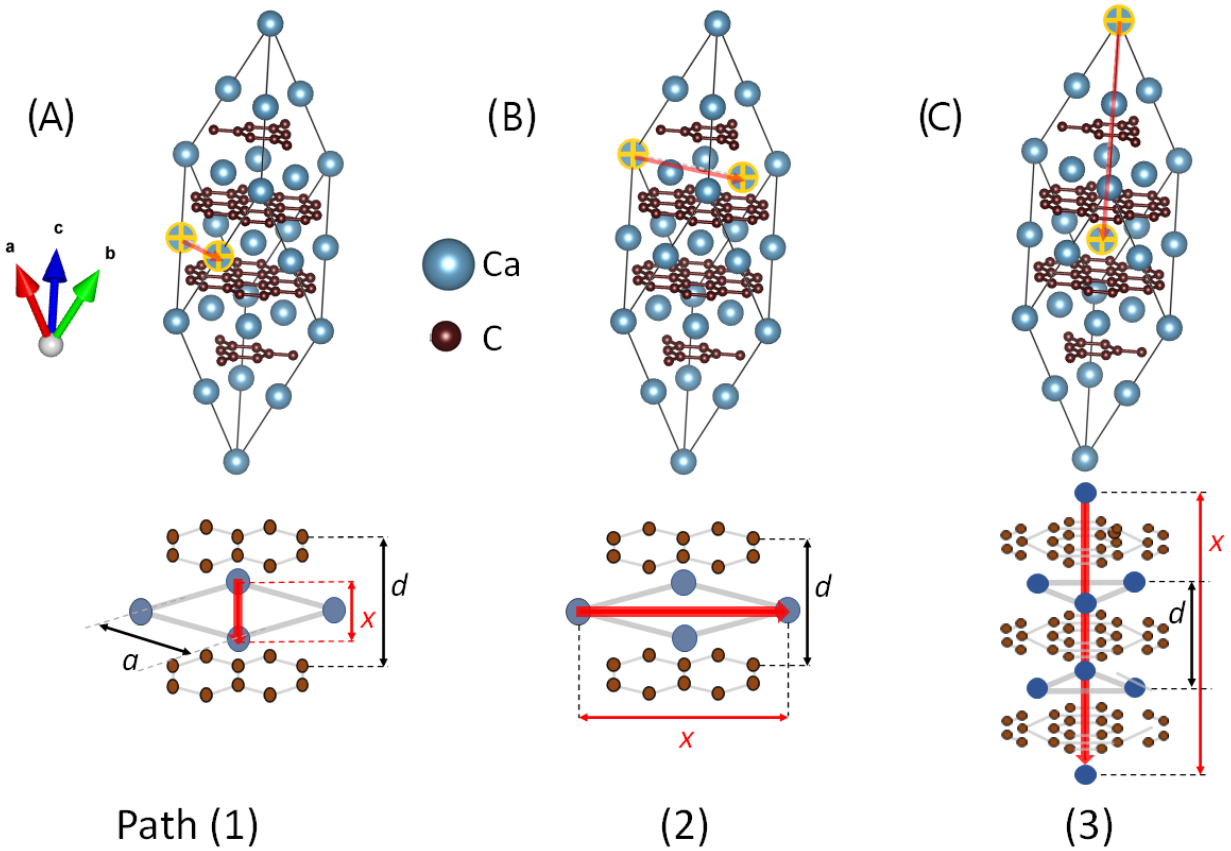


**Figure 2.** (**a**,**b**,**c**): The superconducting paths (1)–(3) for the rhombohedral unit cell of $CaC_6$. (**A**–**C**) present 2 × 2 × 2 supercells; Paths (1), (2), and (3) provide a schematic drawing of each possible superconducting path (marked by red arrows) that allows for proper counting of $N_A$. All colors are identical to Figure 1 Paths (1) and (2) are located within the (*a*,*b*)-plane, path (3) goes along the (*c*)-axis. Note also that especially for path (3) the supercell is still incomplete regarding the full information on the passed, near atoms.

There are three symmetry-equivalent rhombohedral edges, giving a path multiplicity $P$ of

$$P = 3. \tag{5}$$

Near-atom analysis shows that the carbon hexagon lies at a significant distance from this path. None of the carbon atoms satisfy the RH proximity criterion $l/x \leq 0.5$, nor the refined standing-wave criterion as discussed in Ref. [23]. Consequently, no atoms are counted as near atoms for this path. By convention, this corresponds to

$$N_A = 1. \tag{6}$$

### *3.3. Rhombohedral Face-Diagonal Path*

A second class of superconducting paths connects calcium atoms across the faces of the rhombohedral unit cell. These vectors correspond to differences in two rhombohedral basis vectors and are symmetry-allowed within the $R\bar{3}m$ space group, shown in Figure 2B.

The length of this path is

$$x_{\mathrm{R2}} \approx 0.750 \text{ nm}, \tag{7}$$

which coincides numerically with the in-plane diagonal path identified in the hexagonal description.

There are three symmetry-equivalent face-diagonal paths, resulting in a multiplicity

$$P = 3. \tag{8}$$

In this configuration, the superconducting path passes close to multiple carbon atoms belonging to adjacent graphene layers. Applying the refined RH proximity criterion based on the standing-wave model yields a total number of near atoms

$$N_A = 14. \tag{9}$$

This path represents the dominant in-plane superconducting channel within the rhombohedral description.

### *3.4. Rhombohedral Body-Diagonal Path*

The longest symmetry-allowed superconducting path in rhombohedral $CaC_6$ connects calcium atoms along a body-diagonal-like direction of the rhombohedral cell. This path spans three consecutive graphene layers and corresponds to the interlayer superconducting channel, shown in Figure 2C.

The path length is

$$x_{\mathrm{R3}} \approx 1.357 \text{ nm}. \tag{10}$$

Only one such path exists per calcium atom, yielding a multiplicity

$$P = 1. \tag{11}$$

Along this path, the Cooper pairs encounter multiple carbon layers as well as triangular arrangements of calcium atoms in adjacent planes. The symmetry of the calcium triangles ensures that the path is RH-allowed. Detailed near-atom counting, including contributions from three distinct carbon layers, yields a large number of near atoms,

$$N_A = 52. \tag{12}$$

This path provides the dominant out-of-plane superconducting contribution in $CaC_6$.

### *3.5. Summary of Rhombohedral RH Paths*

Table 1 summarizes the superconducting paths identified in the rhombohedral description of $CaC_6$.

**Table 1.** Roeser–Huber superconducting paths in rhombohedral $CaC_6$.

| Path | Description | $x$ (nm) | $P$ | $N_A$ |
|---|---|---|---|---|
| $R_1^{\mathrm{rhomb}}$ | rhombohedral edge | 0.517 | 3 | 1 |
| $R_2^{\mathrm{rhomb}}$ | face diagonal | 0.750 | 3 | 14 |
| $R_3^{\mathrm{rhomb}}$ | body diagonal | 1.357 | 1 | 52 |

The three superconducting paths identified here form the complete set of symmetry-allowed RH channels in the primitive rhombohedral description of $CaC_6$. This now enables the calculation of the various $T_c^{(\mathrm{calc})}$ to be performed.

Table 2 summarizes the RH calculation of rhomohedral $CaC_6$. The calcium atoms donate their two outer electrons to the graphene, so $N_L = 2$ [23]. $T_c^{\mathrm{calc}}$ is obtained from the sum of directions (1) + (2), so 10.8 K. This value is quite similar to the one of the *c*-axis direction (path 3) but is only slightly larger.

**Table 2.** Calculation of $T_c$ of $CaC_6$ in the rhombohedral description using the RH formalism (Equation (1)).

| Direction | $x$ [nm] | $N_L$ | $N_A$ | $M_{\mathrm{L}}$ $[\eta m_e]$ | $\Delta_{(0)}$ [meV] | $T_c^{(\mathrm{calc})}$ [K] |
|---|---|---|---|---|---|---|
| (1), *(a,b)* | 0.517 | 2 | 1 | 2 | 0.383 | 1.4 |
| (2), *(a,b)* | 0.750 | 2 | 14 | 0.1429 | 2.549 | 9.4 |
| (3), *(c)* | 1.357 | 2 | 52 | 0.0385 | 2.891 | 10.7 |

In the following section, these paths are mapped onto their counterparts in the hexagonal description, where the same superconducting channels appear in an unfolded and geometrically more transparent form.

## 4. Superconducting Paths in Hexagonal $CaC_6$

The possible superconducting paths for the hexagonal representation of $CaC_6$ were discussed in detail in Ref. [23]. Thus, we give here a short summary of the findings.

In the hexagonal representation of $CaC_6$, the unit cell contains three calcium atoms and eighteen carbon atoms arranged in alternating calcium planes and graphene layers. This non-primitive description does not introduce additional superconducting channels but rather unfolds the symmetry-equivalent paths of the primitive rhombohedral lattice into a geometrically transparent form. The hexagonal description is therefore particularly useful for visualizing the geometry of these paths and for performing detailed near-atom counting, especially in the presence of multiple carbon layers.

### *4.1. In-Plane Edge Paths (Hexagonal)*

The shortest Ca–Ca connections in the hexagonal unit cell lie along the edges of the $(a, b)$ plane. These paths connect calcium atoms within the same calcium layer and have a length

$$x_{\mathrm{H1}} = a_{\mathrm{hex}} \approx 0.433\ \mathrm{nm}. \tag{13}$$

These in-plane edge paths do not correspond to a single rhombohedral lattice vector but arise from the unfolding of the rhombohedral edge paths (R1) into the expanded

hexagonal cell. Taken individually, these paths are shorter than the rhombohedral R1 path; however, collectively, they represent the same superconducting channel.

A detailed geometric analysis shows that no carbon or calcium atoms satisfy the RH proximity criteria for these paths. Consequently, the near-atom count is

$$N_A = 1, \tag{14}$$

consistent with the rhombohedral description.

### *4.2. In-Plane Diagonal Path (Hexagonal)*

A second symmetry-allowed superconducting path lies along the diagonal of the hexagonal $(a, b)$ plane. This path connects calcium atoms in adjacent positions within the same plane and has a length

$$x_{\mathrm{H2}} = \sqrt{3}\, a_{\mathrm{hex}} \approx 0.750 \text{ nm}. \tag{15}$$

This path is the direct hexagonal counterpart of the rhombohedral face-diagonal path (R2). In contrast to the rhombohedral representation, the hexagonal cell makes the surrounding carbon layers explicit, allowing a layer-resolved analysis of near atoms.

Applying the refined RH proximity criterion based on the standing-wave model reveals multiple carbon atoms in adjacent graphene layers that interact with the Cooper pairs. The total number of near atoms is

$$N_A = 14, \tag{16}$$

in exact agreement with the rhombohedral analysis.

This in-plane diagonal path constitutes the dominant in-plane superconducting channel in $CaC_6$.

### *4.3. Out-of-Plane (c-Axis) Path (Hexagonal)*

The longest superconducting path in the hexagonal description runs along the $c$ axis, connecting calcium atoms in successive calcium layers. The path length is

$$x_{\mathrm{H3}} = c_{\mathrm{hex}} \approx 1.357 \text{ nm}. \tag{17}$$

This path represents the unfolded form of the rhombohedral body-diagonal path (R3). In the hexagonal representation, the triangular arrangement of calcium atoms in adjacent layers is explicitly visible. The centers of these triangles define the superconducting path, ensuring that the path remains RH-allowed despite the absence of a calcium atom directly on the path.

Along this path, the Cooper pairs encounter three distinct graphene layers as well as calcium triangles in intermediate planes. The hexagonal geometry allows these contributions to be counted directly. Applying the refined RH criteria yields a total near-atom count of

$$N_A = 52. \tag{18}$$

This path provides the dominant out-of-plane contribution to superconductivity in $CaC_6$.

### *4.4. Summary of Hexagonal RH Paths*

Table 3 summarizes the superconducting paths identified in the hexagonal representation and explicitly indicates their correspondence to the rhombohedral paths discussed above.

**Table 3.** Roeser–Huber superconducting paths in hexagonal $CaC_6$ and their relation to rhombohedral paths.

| Hexagonal Path | Direction | $x$ (nm) | $P$ | $N_A$ | Rhombohedral Origin |
|---|---|---|---|---|---|
| $R_1^{\mathrm{hex}}$ | in-plane edge | 0.433 | unfolded | 1 | $R_1^{\mathrm{rhomb}}$ |
| $R_2^{\mathrm{hex}}$ | in-plane diagonal | 0.750 | identical | 14 | $R_2^{\mathrm{rhomb}}$ |
| $R_3^{\mathrm{hex}}$ | $c$ axis | 1.357 | unfolded | 52 | $R_3^{\mathrm{rhomb}}$ |

The hexagonal description thus provides a geometrically intuitive visualization of superconducting paths and near-atom environments without introducing new RH channels. All superconducting properties derived from the hexagonal representation can be traced back uniquely to the primitive rhombohedral superconducting paths.

Table 4 summarizes the calculations for $CaC_6$ in its hexagonal representation as discussed in Ref. [23]. $T_c^{(\mathrm{calc})}$ in the $(a,b)$-plane was determined to be the sum of directions (1) and (2), so $T_c^{(\mathrm{calc})} = 11.4$ K, which is larger than the result of the rhombohedral analysis but still close to the experimentally determined values of $T_c$.

**Table 4.** Calculation of $T_c$.

| Direction | $x$ [nm] | $N_L$ | $N_A$ | $M_{\mathrm{L}}$ $[\eta m_e]$ | $\Delta_{(0)}$ [meV] | $T_c^{(\mathrm{calc})}$ [K] |
|---|---|---|---|---|---|---|
| (1), *(a,b)* | 0.433 | 2 | 1 | 2 | 0.546 | 2.0 |
| (2), *(a,b)* | 0.750 | 2 | 14 | 0.1429 | 2.549 | 9.4 |
| (3), *(c)* | 1.357 | 2 | 52 | 0.0385 | 2.891 | 10.7 |

## 5. Mapping Between Rhombohedral and Hexagonal Superconducting Paths

Within the Roeser–Huber (RH) formalism, superconducting paths are defined as translationally closed vectors that connect symmetry-equivalent calcium atoms. In the rhombohedral $R\bar{3}m$ structure of $CaC_6$, the primitive unit cell contains one calcium atom and six carbon atoms. Consequently, all allowed RH paths are determined solely by the primitive rhombohedral lattice vectors.

In this primitive description [36,37] three symmetry-distinct translational paths satisfy the RH criteria:

$$R_1 = \mathbf{a}_1, \qquad R_2 = \mathbf{a}_1 - \mathbf{a}_2, \qquad R_3 = \mathbf{a}_1 + \mathbf{a}_2 + \mathbf{a}_3. \tag{19}$$

These correspond to the rhombohedral edge, face diagonal, and body diagonal of the primitive cell, respectively. Their lengths depend only on the rhombohedral lattice parameters and define the complete set of superconducting channels in the primitive structure.

For visualization and comparison with earlier literature, it is convenient to express these paths in the hexagonal setting. The hexagonal unit cell is a non-primitive conventional cell containing three calcium atoms and eighteen carbon atoms. Its lattice vectors are related to the rhombohedral basis by the standard crystallographic transformation,

and each rhombohedral RH path can therefore be expressed as an integer combination of the hexagonal lattice vectors.

Because the hexagonal cell is an unfolded representation of the primitive rhombohedral lattice, the mapping between the two descriptions is not always one-to-one at the level of individual vectors. Instead, a single rhombohedral superconducting path may appear as one or several geometrically distinct but symmetry-equivalent paths in the hexagonal representation. Nevertheless, the complete set of RH superconducting channels remains invariant.

### *5.1. Rhombohedral Edge Path*

The rhombohedral edge path $R_1^{\text{rhomb}}$ connects calcium atoms along one of the primitive lattice vectors. In the hexagonal representation, this path does not appear as a single translational vector of the conventional cell. Instead, it is unfolded into several shorter in-plane Ca–Ca connections along the edges of the hexagonal lattice.

These hexagonal edge segments are sublattice translations that exist only because the conventional cell contains three calcium atoms. They do not represent independent RH paths in the primitive lattice. When considered collectively, however, they reproduce the same superconducting channel as the rhombohedral edge path.

In both descriptions, the path passes no additional atoms within the RH proximity radius, yielding

$$N_A = 1. \tag{20}$$

### *5.2. Rhombohedral Face-Diagonal Path*

The rhombohedral face-diagonal path $R_2^{\text{rhomb}}$ corresponds directly to the in-plane diagonal path in the hexagonal representation. In both coordinate systems, the superconducting channel lies within the basal plane and has the same geometric length,

$$x \approx 0.750 \text{ nm}. \tag{21}$$

The hexagonal description makes the stacking of the graphene layers more explicit, allowing a transparent identification of the near-atom planes contributing to the RH proximity count. Applying the refined RH criterion yields

$$N_A = 14 \tag{22}$$

in both representations. Thus, $R_2^{\text{rhomb}}$ and the hexagonal in-plane diagonal represent the same superconducting channel expressed in different coordinate systems.

### *5.3. Rhombohedral Body-Diagonal Path*

The rhombohedral body-diagonal path $R_3^{\text{rhomb}}$ corresponds to the out-of-plane superconducting channel along the hexagonal $c$ axis. In the primitive rhombohedral lattice, this path is a single long translation connecting equivalent calcium atoms across multiple unit cells.

In the hexagonal representation, the same channel appears as a sequence of Ca–Ca connections between stacked calcium planes. The triangular arrangement of calcium atoms in adjacent layers becomes explicit, and the centers of these triangles define the superconducting trajectory. The surrounding graphene sheets form several distinct near-atom planes whose contributions can be counted directly.

Despite these geometric differences, the RH proximity count remains identical in both representations,

$$N_A = 52. \tag{23}$$

### *5.4. Summary of the Mapping*

Table 5 summarizes the correspondence between the rhombohedral and hexagonal RH superconducting paths.

**Table 5.** Roeser–Huber superconducting paths in hexagonal $CaC_6$ and their relation to rhombohedral paths.

| Rhombohedral Path | Hexagonal Counterpart | $x$ (nm) | $P$ | $N_A$ | Channel |
|---|---|---|---|---|---|
| $R_1^{\mathrm{rhomb}}$ (edge) | unfolded in-plane edges | 0.517 | 3 | 1 | weak in-plane |
| $R_2^{\mathrm{rhomb}}$ (face diag.) | in-plane diagonal | 0.750 | 3 | 14 | dominant in-plane |
| $R_3^{\mathrm{rhomb}}$ (body diag.) | $c$-axis path | 1.357 | 1 | 52 | dominant out-of-plane |

In both representations, the same three superconducting channels are obtained, with identical near-atom environments, confirming that the RH path topology is independent of the crystallographic setting. While individual superconducting paths differ geometrically between the rhombohedral and hexagonal descriptions, the complete set of symmetry-allowed RH channels—and therefore the predicted superconducting properties—remains unchanged. This invariance confirms that the RH formalism captures intrinsic structural features of superconductivity rather than artifacts of unit-cell choice.

## 6. Discussion

Although the rhombohedral and hexagonal descriptions of $CaC_6$ are crystallographically equivalent, they differ substantially in their geometric representation of atomic connectivity. In particular, individual superconducting paths defined within the Roeser–Huber (RH) formalism are not identical vectors in the two descriptions. Nevertheless, when all symmetry-equivalent paths are taken into account, both representations yield the same set of effective superconducting channels.

*Metric Dependence of RH Path Counting*

For $CaC_6$, the hexagonal and primitive rhombohedral descriptions represent the same Bravais lattice but differ in their metric realization. Wang et al. [18,19] showed the formulae connecting the reciprocal hexagonal and rhombohedral lattices of $CaC_6$. Here, we follow the description of Refs. [36,37].

Let $\mathbf{a}_1^{\mathrm{hex}}$, $\mathbf{a}_2^{\mathrm{hex}}$, and $\mathbf{c}^{\mathrm{hex}}$ denote the conventional hexagonal basis vectors. The primitive rhombohedral basis vectors may be written as

$$\mathbf{a}_1^{\mathrm{rh}} = \frac{1}{3}\left(\mathbf{a}_1^{\mathrm{hex}} + \mathbf{a}_2^{\mathrm{hex}} + \mathbf{c}^{\mathrm{hex}}\right), \tag{24}$$

with cyclic permutations generating $\mathbf{a}_{2,3}^{\mathrm{rh}}$. The corresponding primitive length is

$$a_{\mathrm{rh}} = \left|\mathbf{a}_1^{\mathrm{rh}}\right| \approx 0.517\ \mathrm{nm}. \tag{25}$$

In the hexagonal metric, three RH paths satisfy translational closure: a short in-plane sublattice path

$$L_1^{\mathrm{hex}} = \frac{\sqrt{3}}{3} a_{\mathrm{hex}} \approx 0.433\ \mathrm{nm}, \tag{26}$$

a longer in-plane lattice path $L_2^{\mathrm{hex}} \approx 0.750$ nm, and an axial path $L_3 = c \approx 1.357$ nm. All three contribute to Equation (1) in the hexagonal description.

Upon transformation to the primitive rhombohedral metric, the shortest in-plane path $L_1^{\mathrm{hex}}$ no longer satisfies the translational closure condition,

$$\mathbf{L}_1^{\mathrm{hex}} \notin \mathrm{Span}_{\mathbb{Z}}\left\{\mathbf{a}_1^{\mathrm{rh}}, \mathbf{a}_2^{\mathrm{rh}}, \mathbf{a}_3^{\mathrm{rh}}\right\}, \tag{27}$$

and is therefore excluded as a primary RH resonance. The shortest admissible in-plane path becomes the primitive rhombohedral vector,

$$L_1^{\mathrm{rh}} = a_{\mathrm{rh}} \approx 0.517\ \mathrm{nm}, \tag{28}$$

while the longer in-plane and axial paths remain invariant,

$$L_2^{\mathrm{rh}} = L_2^{\mathrm{hex}}, \qquad L_3^{\mathrm{rh}} = L_3^{\mathrm{hex}}. \tag{29}$$

As a consequence, the total number of effective superconducting channels remains 3, but their metric weights in Equation (1) are redistributed. Since $T_{c,i} \propto L_i^{-2}$, the replacement of the hexagonal sublattice path by the longer primitive rhombohedral vector reduces its contribution, thereby altering the relative balance between in-plane and axial resonances slightly affecting the total $T_c$.

This analysis demonstrates that RH path counting is invariant under changes in lattice description only when translational closure is enforced in the appropriate metric, with sublattice-only resonances contributing exclusively in representations that explicitly resolve the corresponding sublattice symmetry.

Although the calculated superconducting transition temperature yields quite reasonable agreement with experiments for a given material, a small variation in $T_c^{(\mathrm{calc})}$ is observed between the rhombohedral and hexagonal representations of $CaC_6$. The difference obtained here amounts to approximately 5.4%, which is well within an acceptable margin for a structure-based model of this type.

At the same time, the present results suggest a somewhat different perspective on the RH formalism. Rather than focusing primarily on the numerical value of the calculated transition temperature, the analysis highlights the structural path-counting logic as the central and most robust component of the approach. This viewpoint emphasizes the geometric resonance concept itself while treating the final $T_c$ evaluation as a secondary step that may still require further theoretical refinement.

The core element of the RH formalism is the geometrical counting scheme of passed and near atoms along symmetry-allowed superconducting paths. This counting logic constitutes the physically decisive part of the approach, as it determines the effective resonance environment experienced by the superconducting wave. According to Equation (1), a shorter resonance length $x$ generally leads to a higher $T_c^{(\mathrm{calc})}$. However, as demonstrated in the present case, longer paths may involve a larger number of passed, near atoms ($N_A$) participating in the superconductivity, which can result in an even higher $T_c^{(\mathrm{calc})}$. A striking example of this effect is provided by the extreme case of $LaH_{10}$ under pressure, as discussed recently in Ref. [38].

In contrast, the final conversion of these geometrical quantities into a numerical value of the transition temperature $T_c$ still involves intermediate steps whose microscopic theoretical foundations are not yet fully established.

Nevertheless, the present analysis demonstrates that the RH formalism provides a consistent framework for treating crystals described in different, yet crystallographically equivalent, unit-cell representations. As shown for $CaC_6$, identical physical conclusions are obtained when the formalism is applied to both the primitive rhombohedral and the conventional hexagonal descriptions, provided that all symmetry-equivalent paths are

properly identified and counted. This confirms that the RH construction is invariant with respect to the choice of crystallographic setting, as long as the underlying space-group symmetry relations are preserved.

At the same time, the case of $CaC_6$ illustrates the practical limitations of purely visual inspection and manual determination of the near-atom number $N_A$. Even for a comparatively simple layered compound, systematic path identification and symmetry-consistent counting require careful bookkeeping. For more complex crystal structures, manual procedures become rapidly impractical and potentially error-prone. This observation strongly motivates the implementation of automated algorithms that perform symmetry-resolved path searches and near-atom counting directly from crystallographic input data.

The same geometric reasoning can be extended to genuine polymorphic systems, such as lanthanum or mercury, where distinct crystal structures correspond to different superconducting transition temperatures, as discussed in Ref. [23]. Within the RH framework, such variations can be interpreted naturally in terms of changes in the set of available resonance paths and modifications of their local atomic environments. In this way, structural phase transitions translate directly into modifications of the resonance condition.

As noted in the Introduction, $LiC_6$ represents the closest structural analogue to $CaC_6$. Application of the RH formalism to $LiC_6$ yields a calculated transition temperature $T_c^{\mathrm{calc}} \sim 8.1$ K for the $(a, b)$-plane (with $\Delta_{(0)} = 2.21$ meV), in close agreement with the theoretical prediction reported in Ref. [12]. This result indicates that the $LiC_6$ unit cell is, in principle, capable of supporting a symmetry-consistent superconducting carrier wave within the RH construction. The agreement with independent theoretical estimates provides additional support for the internal consistency of the approach.

From a broader perspective, the present results indicate that the Roeser–Huber (RH) formalism provides a compact, physically motivated descriptor of superconducting materials that is well suited for integration into data-driven approaches. Unlike purely compositional or electronic descriptors, the RH parameters are directly derived from crystallographic geometry and encode the essential structural features that govern superconducting pathways, namely the translational path length, multiplicity, and near-atom environment. As all these quantities can be computed automatically from crystallographic input, they form a low-dimensional and interpretable feature set suitable for integration into data-driven approaches.

In particular, RH-derived quantities could serve as structured input features in machine learning models for superconductivity prediction. Their explicit connection to symmetry and real-space connectivity may enhance model interpretability compared to purely statistical descriptors. In this sense, the RH formalism offers a possible bridge between physically grounded analytical models and statistical learning strategies, enabling hybrid approaches in which symmetry-allowed superconducting channels guide large-scale materials screening.

Accordingly, the RH framework may serve as a useful predictive tool for the structural design and screening of new graphite intercalation compounds [16], as well as for broader classes of superconducting materials.

## 7. Conclusions

We have performed a systematic Roeser–Huber analysis of superconducting paths in $CaC_6$ using both rhombohedral and hexagonal crystallographic descriptions. Although the individual superconducting paths differ geometrically between the two representations, direct mapping demonstrates that all RH parameters—including multiplicities and near-atom counts—are invariant with respect to the choice of unit cell. The hexagonal description, while non-primitive, provides enhanced geometric transparency for identifying super-

conducting paths and performing near-atom counting. These results establish the representation independence of the RH formalism and confirm that its predictions are rooted in intrinsic structural features rather than artifacts of crystallographic choice. This work provides a robust foundation for extending the RH analysis to more complex superconducting systems and stimulates the use of the RH formalism in machine learning approaches screening materials databases.

**Author Contributions:** Conceptualization, M.R.K.; Formal Analysis, A.K.-V. and M.R.K.; Investigation, A.K.-V. and M.R.K.; Visualization, A.K.-V. and M.R.K.; Writing—Original Draft Preparation, M.R.K.; Writing—Review and Editing, A.K.-V. and M.R.K. All authors have read and agreed to the published version of the manuscript.

**Funding:** The work in Saarbrücken was partly subsided by the SUPERFOAM international project funded by ANR and DFG under references ANR-17-CE05-0030 and DFG-ANR Ko2323-10, which is gratefully acknowledged.

**Institutional Review Board Statement:** Not applicable.

**Informed Consent Statement:** Not applicable.

**Data Availability Statement:** The original contributions presented in this study are included in the article. Further inquiries can be directed to the corresponding author.

**Conflicts of Interest:** Authors Michael R. Koblischka and Anjela Koblischka-Veneva are the co-founders of the consulting company Supra Saar. The authors declare no conflicts of interest.

## References

1. Dresselhaus, M.S.; Dresselhaus, G. Intercalation compounds of graphite. *Adv. Phys.* **1981**, *30*, 139–326. [CrossRef]
2. Enoki, T.; Suzuki, M.; Endo, M. *Graphite Intercalation Compounds and Applications*; Oxford University Press: Oxford, UK, 2003.
3. Smith, R.P.; Weller, T.E.; Howard, C.A.; Dean, M.P.M.; Rahnejat, K.C.; Saxena, S.S.; Ellerby, M. Superconductivity in graphite intercalation compounds. *Physica C* **2015**, *514*, 50–58. [CrossRef]
4. Weller, T.E.; Ellerby, M.; Saxena, S.S.; Smith, R.P.; Skipper, N.T. Superconductivity in the intercalated graphite compounds $C_6$Yb and $C_6$Ca. *Nat. Phys.* **2005**, *1*, 39–41. [CrossRef]
5. Emery, N.; Hérold, C.; Lagrange, P. Structural study and crystal chemistry of the first stage calcium graphite intercalation compound. *J. Solid State Chem.* **2005**, *178*, 2947–2952. [CrossRef]
6. Emery, N.; Hérold, C.; d'Astuto, M.; Garcia, V.; Bellin, C.; Marêché, J.F.; Lagrange, P.; Loupias, G. Superconductivity of Bulk $CaC_6$. *Phys. Rev. Lett.* **2005**, *95*, 087003. [CrossRef]
7. Emery, N.; Hérold, C.; Marêché, J.-F.; Lagrange, P. Synthesis and superconducting properties of $CaC_6$. *Sci. Technol. Adv. Mater.* **2008**, *9*, 044102. [CrossRef]
8. Calandra, M.; Mauri, F. Theoretical Explanation of Superconductivity in $C_6$Ca. *Phys. Rev. Lett.* **2005**, *95*, 237002. [CrossRef] [PubMed]
9. Ludbrook, B.M.; Levy, G.; Nigge, P.; Zonno, M.; Schneider, M.; Dvorak, D.J.; Veenstra, C.N.; Zhdanovich, S.; Wong, D.; Dosanjh, P.; et al. Evidence for superconductivity in Li-decorated monolayer graphene. *Proc. Natl. Acad. Sci. USA* **2015**, *112*, 11795–11799. [CrossRef]
10. Gholami, R.; Moradian, R.; Moradian, S.; Pickett, W.E. Superconducting Phases in Lithium Decorated Graphene $LiC_6$. *Sci. Rep.* **2018**, *8*, 13795. [CrossRef]
11. Sergeyev, D.; Duisenova, A.; Embergenov, Z. Modeling of electrotransport properties of Li-intercalated graphene film. *J. Phys. Conf. Ser.* **2021**, *2140*, 012025. [CrossRef]
12. Profeta, G.; Calandra, M.; Mauri, F. Phonon-mediated superconductivity in graphene by lithium deposition. *Nat. Phys.* **2012**, *8*, 131–134. [CrossRef]
13. Csányi, G.; Littlewood, P.B.; Nevidomskyy, A.H.; Pikard, C.P.; Simons, B.D. The role of the interlayer state in the electronic structure of superconducting graphite intercalated compounds. *Nat. Phys.* **2005**, *1*, 42–45. [CrossRef]
14. Lamura, G.; Aurino, M.; Cifariello, G.; Gennaro, E.D.; Andreone, A.; Emery, N.; Hérold, C.; Marêché, J.-F.; Lagrange, P. Experimental Evidence of s-Wave Superconductivity in Bulk $CaC_6$. *Phys. Rev. Lett.* **2006**, *96*, 107008. [CrossRef]
15. Gauzzi, A.; Takashima, S.; Takeshita, N.; Terakura, C.; Takagi, H.; Emery, N.; Hérold, C.; Lagrange, P.; Loupias, G. Enhancement of Superconductivity and Evidence of Structural Instability in Intercalated Graphite $CaC_6$ under High Pressure. *Phys. Rev. Lett.* **2007**, *98*, 067002. [CrossRef]

16. Kawaguchi, N.; Shibata, K.; Mizoguchi, T. Possible New Graphite Intercalation Compounds for Superconductors and Charge Density Wave Materials: Systematic Simulations with Various Intercalants Using a van der Waals Density Functional Method. *J. Phys. Chem. C* **2023**, *127*, 9833–9843. [CrossRef]
17. d'Astuto, M.; Calandra, M.; Bendiab, N.; Loupias, G.; Mauri, F.; Zhou, S.; Graf, J.; Lanzara, A.; Emery, N.; Hérold, C.; et al. Phonon dispersion and low-energy anomaly in $CaC_6$ from inelastic neutron and x-ray scattering experiments. *Phys. Rev. B* **2010**, *81*, 104519. [CrossRef]
18. Wang, B.; Bianconi, A.; Mackinnon, I.D.R.; Alarco, J.A. Superlattice delineated Fermi surface nesting and electron-phonon coupling in $CaC_6$. *Crystals* **2024**, *14*, 499. [CrossRef]
19. Wang, B.; Bianconi, A.; Mackinnon, I.D.R.; Alarco, J.A. Superlattice Symmetries Reveal Electronic Topological Transition in $CaC_6$ with Pressure. *Crystals* **2024**, *14*, 554. [CrossRef]
20. Roeser, H.P.; Haslam, D.T.; Lopez, J.S.; Stepper, M.; von Schoenermark, M.F.; Huber, F.M.; Nikoghosyan, A.S. Correlation between transition temperature and crystal structure of niobium, vanadium, tantalum and mercury superconductors. *Acta Astronaut.* **2010**, *67*, 1333–1336. [CrossRef]
21. Koblischka, M.R.; Roth, S.; Koblischka-Veneva, A.; Karwoth, T.; Wiederhold, A.; Zeng, X.L.; Fasoulas, S.; Murakami, M. Relation between Crystal Structure and Transition Temperature of Superconducting Metals and Alloys. *Metals* **2020**, *10*, 158. [CrossRef]
22. Koblischka, M.R.; Koblischka-Veneva, A. Calculation of $T_c$ of Superconducting Elements with the Roeser–Huber Formalism. *Metals* **2022**, *12*, 337. [CrossRef]
23. Koblischka, M.R.; Koblischka-Veneva, A. Superconductivity in the Intercalated Graphite Compound $CaC_6$ and the Roeser–Huber Formalism. *Metals* **2025**, *15*, 1367. [CrossRef]
24. Rohlf, J.W. *Modern Physics from α to* $Z^0$; Wiley: New York, NY, USA, 1994.
25. Buckel, W.; Kleiner, R. *Supraleitung. Grundlagen und Anwendungen*, 7th ed.; Wiley-VCH: Weinheim, Germany, 2013. (In German)
26. Stewart, G.R. Superconductivity in the A15 structure. *Physica C* **2015**, *514*, 28–35. [CrossRef]
27. ICDD. *ICDD PDF Data Base*; ICDD: Newtown Square, PA, USA, 2025.
28. Materials Project Database V2019.05. Available online: https://materialsproject.org/ (accessed on 15 February 2026).
29. Crystallography Open Database (COD). Available online: https://www.crystallography.net/cod/index.php (accessed on 15 February 2026).
30. Merchant, A.; Batzner, S.; Schoenholz, S.S.; Aykol, M.; Cheon, G.; Cubuk, E.D. Scaling deep learning for materials discovery. *Nature* **2023**, *624*, 80–85. [CrossRef]
31. Gashmard, H.; Shakeripour, H.; Alaei, M. Predicting superconducting transition temperature through advanced machine learning and innovative feature engineering. *Sci. Rep.* **2024**, *14*, 3965. [CrossRef]
32. Zeni, C.; Pinsler, R.; Zügner, D.; Fowler, A.; Horton, M.; Fu, X.; Wang, Z.; Shysheya, A.; Crabbé, J.; Ueda, S.; et al. A generative model for inorganic materials design. *Nature* **2025**, *639*, 624–632. [CrossRef]
33. Adiga, S.; Waghmare, U.V. Accelerating the Search for Superconductors Using Machine Learning. *Comput. Mater. Sci.* **2026**, *263*, 114453. [CrossRef]
34. CrystalMaker Software Ltd., Begbroke, Oxfordshire, OX5 1PF, UK. Available online: https://crystalmaker.com/ (accessed on 15 February 2026).
35. Momma, K.; Izumi, F. VESTA 3 for three-dimensional visualization of crystal, volumetric and morphology data. *J. Appl. Crystallogr.* **2011**, *44*, 1272–1276. [CrossRef]
36. ITA. *International Tables for Crystallography, Volume A: Space-Group Symmetry*, 5th ed.; Springer: Berlin/Heidelberg, Germany, 2005.
37. QuantumATK Manual and Homepage. Available online: https://docs.quantumatk.com/tutorials/rhombo_hex_trigonal/rhombo_hex_trigonal.html (accessed on 15 February 2026).
38. Koblischka, M.R.; Koblischka-Veneva, A. Calculating the Transition Temperature of Metal-Hydrogen Systems Using the Roeser-Huber Formalism. *Phys. Met. Metallogr.* **2025**, *126*, 1138–1143. [CrossRef]